FULL PAPER

Calibration-free regional RF shims for MRS

Adam Berrington[1] | Michal Považan[2,3] | Christopher Mirfin[1] | Stephen Bawden[1] |
Young Woo Park[4] | Daniel C. Marsh[1] | Richard Bowtell[1] | Penny A. Gowland[1]

[1]Sir Peter Mansfield Imaging Centre, School of Physics and Astronomy, University of Nottingham, Nottingham, UK

[2]Russell H. Morgan Department of Radiology, Johns Hopkins University School of Medicine, Baltimore, MD, USA

[3]F. M. Kirby Research Center for Functional Brain Imaging, Kennedy Krieger Institute, Baltimore, MD, USA

[4]Center for Magnetic Resonance Research, Department of Radiology, University of Minnesota Medical School, Minneapolis, MN, USA

Correspondence
Adam Berrington, Sir Peter Mansfield Imaging Centre, School of Physics and Astronomy, University of Nottingham, Nottingham, UK.
Email: adam.berrington@nottingham.ac.uk

Purpose: Achieving a desired RF transmit field (B_1^+) in small regions of interest is critical for single-voxel MRS at ultrahigh field. Radio-frequency (RF) shimming, using parallel transmission, requires B_1^+ mapping and optimization, which limits its ease of use. This work aimed to generate calibration-free RF shims for predefined target regions of interest, which can be applied to any participant, to produce a desired absolute magnitude B_1^+ ($|B_1^+|$).

Methods: The RF shims were found offline by joint optimization on a database comprising B_1^+ maps from 11 subjects, considering regions of interest in occipital cortex, hippocampus and posterior cingulate, as well as whole brain. The $|B_1^+|$ achieved was compared with a tailored shimming approach, and MR spectra were acquired using tailored and calibration-free shims in 4 participants. Global and local $10g$ specific-absorption-rate deposition were estimated using Duke and Ella dielectric models.

Results: There was no difference in the mean $|B_1^+|$ produced using calibration-free versus tailored RF shimming in the occipital cortex ($p = .15$), hippocampus ($p = .5$), or posterior cingulate ($p = .98$), although differences were observed in the RMS error $|B_1^+|$. Spectra acquired using calibration-free shims had similar SNR and low residual water signal. Under identical power settings, specific-absorption-rate deposition was lower compared with operating in quadrature mode. For example, the total head specific absorption rate was around 35% less for the occipital cortex.

Conclusion: This work demonstrates that static RF shims, optimized offline for small regions, avoid the need for B_1^+ mapping and optimization for each region of interest and participant. Furthermore, power settings may be increased when using calibration-free shims, to better take advantage of RF shimming.

KEYWORDS

7 T, B_1^+, MR spectroscopy, parallel transmission, RF shimming, universal

1 | INTRODUCTION

Magnetic resonance acquisition at ultrahigh field strengths ($\geq$ 7 T) is challenging, largely because of the inhomogeneity in the RF transmit field (B_1^+). This inhomogeneity arises from the interaction of the relatively short-wavelength RF with the sample, leading to spatial variation in the achieved B_1^+, which in turn causes variations in image contrast.[1,2] A relative loss of B_1^+ in the peripheral brain, when using a volume RF coil, leads to the commonly observed central brightening in brain images. For MRS using small regions of interest (ROIs), a lack of regional B_1^+ can necessitate higher transmit powers or longer duration pulses, thereby prolonging minimum TR or TE. Misadjusted B_1^+ leads to suboptimal flip angles, poor localization, and lower SNR.[3] Thus, increasing the available B_1^+ is critical to obtaining the high spectral quality that is needed to take full advantage of the higher intrinsic SNR and spectral resolution at ultrahigh field.[4,5]

Parallel transmit (pTx) is now available on many MR systems and provides a means to control the B_1^+ profile across a sample.[6-8] B_1^+ can be statically "shimmed" by tailored weighting of RF phase and amplitude on individual transmit (Tx) channels. Strategies to generate RF shim weights for a given ROI include phase-nulling,[9,10] maximum efficiency,[11] and least-squares optimization.[8,12] Use of RF shimming in the brain has been demonstrated in MRSI acquisition[13] and in single-voxel MRS,[10] for example. In the latter work, Emir et al showed that RF shimming provides high spectral quality and improved quantification of metabolites from several ROIs. In practice, RF shimming involves calibration and numerical optimization for each ROI and each participant; mapping of the B_1^+ produced by each Tx channel is needed, as well as the manual definition of a target ROI. This process is time-consuming (~10 minutes per ROI), which limits the use of RF shimming in practice, particularly for clinical studies and when multiple regions are scanned in a single session. Importantly, RF shimming also leads to significant changes in the electric-field distribution, and therefore changes in specific absorption rate (SAR) deposition. Without an ability to monitor or predict SAR deposition, conservative limits are often placed on the allowable transmit power during RF shimming, to avoid generation of high local SAR, and this further diminishes the benefits of RF shimming.

To avoid lengthy pTx calibrations, Gras et al proposed the use of "universal" k_T-point RF pulses for dynamic pTx.[14] These pulses were optimized offline over a database of acquired B_1^+ maps, yet produced similar performance to pulses calculated on a participant-specific basis and required no B_1^+ mapping and numerical optimization on the scanner. This approach relies on the similarity in B_1^+ profiles across participants and has led to development of calibration-free pTx refocusing pulses[15] and selective local excitation pulses.[16] The calibration-free principle has also been extended using machine learning, in which a set of RF pulses was calculated based on clusters of similar participants that better account for intersubject variability.[17] To avoid extensive B_1^+ mapping, Ianni et al developed a machine-learning approach for whole-brain, slice-wise static shimming, requiring only minimal B_1^+ information.[18]

Radiofrequency shimming works best when applied to a small ROI[19]; thus, it is expected that *static* shimming alone may be sufficient for single-voxel MRS. Vendor-provided fixed amplitude and phase settings, calculated using electromagnetic simulations,[20] often cover large ROIs and may be sensitive to variations[21] such as relative position or head size. Thus, to make the benefits of RF shimming more available for spectroscopic acquisition, and given the universal pTx approach,[14] we hypothesized that jointly optimizing RF shim solutions over a database could generate shim weights that can achieve similar target B_1^+ magnitudes, compared with a tailored shimming approach, over a set of small predefined ROIs in any participant. Use of such an approach would account for natural variation across participants and would not require acquisition of B_1^+ maps for each participant.

In this work, therefore, an approach for calibration-free static RF shimming is proposed using anatomical registration and offline optimization over a database of B_1^+ maps. The aim was to generate a desired absolute magnitude of RF transmit field ($|B_1^+|$) within an ROI, without the need for participant-wise B_1^+ mapping and shim calculation. A set of ROIs in commonly investigated brain regions (the occipital cortex [OCC], hippocampus [Hippo], and posterior cingulate cortex [PCC]) was considered. The resulting $|B_1^+|$ and spectra obtained in each ROI using calibration-free shims were compared with those produced using tailored shimming. Additionally, calibration-free RF shims were analyzed in terms of their predicted SAR deposition compared to acquiring with the coil elements–driven quadrature mode.

2 | THEORY

2.1 | *Radiofrequency shimming*

A magnitude least-squares optimization was chosen as the RF shimming strategy. This minimizes the mean squared difference between the shimmed $|B_1^+|$ and a target value over a discrete set of spatial positions covering the ROI. This magnitude least-squares strategy ensures that the mean $|B_1^+|$ in the ROI approaches a target value while inhomogeneity is minimized.

Radiofrequency shimming strategies typically maximize the $|B_1^+|$ field in a region, within constraints on the maximum transmit power, and then renormalize the solution to obtain the desired flip angle. In contrast, in this work, shim solutions were constrained such that transmitted power summed

over all channel elements was limited a priori, to ensure that the sequence will run within (vendor-provided) safety limits for the required pulse shapes and sequence timings. This approach has the advantage that the same shim solution can be applied to every participant, using identical power settings. In addition, the $|B_1^+|$ achieved using different shim solutions can be directly compared with the same fixed total power.[8]

In the following, $|B_1^+|$ is expressed as a ratio of the value measured in the ROI (using B_1^+ mapping) to the prescribed value (ie, the $|B_1^+|$ required to achieve a particular flip angle for a particular amplitude modulated pulse shape, specifically the nominal flip angle of the B_1^+ mapping sequence). Thus, $|B_1^+| = 1$ corresponds to achieving the desired B_1^+ in the ROI.

For each ROI consisting of N_{ROI} discretized points (or image voxels), the RF shim phases and amplitudes applied to each Tx channel can be expressed as a complex $N_c \times 1$ shim vector, w, where N_c is the number of Tx channels. The complex-valued B_1^+ in the ROI is expressed as an $N_{ROI} \times N_c$ transmit sensitivity matrix, S, such that the ith row, s_i, is the concatenation of B_1^+ values at voxel i from all channels. Tailored shimming, performed on a participant-wise basis, involves minimizing the magnitude least squares between the predicted and target $|B_1^+|$ over the ROI, as follows:

$$\min_{w} \left(\frac{1}{N_{ROI}} \sum_{i=1}^{N_{ROI}} \left(|s_i w| - 1 \right)^2 \right) \quad \text{subject to: } w^H w = const. \quad (1)$$

The RF shim weights are calculated subject to a fixed total power, which is equal to that of quadrature mode in which individual channel amplitudes are equal to unity (so $w^H w$8 for an eight-channel system[8]).

2.2 | Joint optimization over the database

Similar to the formulation for universal k_T-point pulses,[14] calibration-free shims were found for each ROI by calculating the shim vector, w, which, when applied to each subject, k, in a database of K subjects, minimizes the error for the worst-case subject in a minimax approach, as follows:

$$\min_{w} \max_{1 \leq k \leq K} \left(\frac{1}{N_{ROI,k}} \sum_{i=1}^{N_{ROI,k}} \left(|s_i^k w| - 1 \right)^2 \right) \quad \text{subject to: } w^H w = const.$$
$$(2)$$

3 | METHODS

3.1 | Magnetic resonance scanning

Data were acquired on a 7T Philips Achieva MR system with a commercial pTx head coil (8 Tx/32 receive; Nova Medical, Houston, TX) (Figure 1A). A total of 15 healthy volunteers participated in this study. Written, informed consent was given by participants before scanning. The study was approved by the Faculty of Medicine and Health Sciences Ethics Committee of the University of Nottingham. For all volunteers, the scanning protocol consisted of a T_1-weighted MPRAGE acquisition (1-mm isotropic, TR/TE = 7.1/2.9 ms, TI = 1.1 seconds, acquisition time = 4:08 minutes) and whole-brain B_1^+ mapping using a 3D DREAM (dual refocusing echo acquisition mode)[22] sequence (3.5-mm isotropic, stimulated echo (STE) flip angle (α) = 60º, excitation flip angle (β) = 7º, TR/TE$_{STE}$/TE$_{FID}$ = 2.6/1.1/1.5 ms, acquisition time = 9 seconds) acquired in quadrature mode, transmitting on all channels simultaneously. To obtain complex B_1^+ information for each Tx channel, low flip-angle 3D gradient-echo images (3.5-mm isotropic, TR/TE = 8/6.7 ms, flip angle = 1°, acquisition time = 3:51 minutes) were also acquired while transmitting on each channel separately. The $|B_1^+|$ on each channel was calculated by normalizing the gradient-echo data on each channel to the complex sum over all channels, and then scaling to the $|B_1^+|$ map acquired with DREAM.[23] Transmit phase on each channel was obtained by comparing the phase of the gradient-echo data from each channel to the first channel. When participants were scanned, no special attention was paid to participant head size or position in the coil. Anatomical and B_1^+ transmit data from the first 11 volunteers formed the training database for the calculation of calibration-free shims (D1-D11). The subsequent four data sets formed the test set (T1-T4) and were used to validate the calculated calibration-free RF shim settings. Demographics of the database and test sets were 28 ± 5 years (5 females) and 47 ± 12 years (2 females), respectively.

3.2 | Region-of-interest definition within the database

Target ROIs for three commonly measured regions in MRS were defined on the Montreal Neurological Institute (MNI) 1-mm brain atlas, namely, OCC ($20 \times 20 \times 20$ mm^3), left Hippo ($30 \times 15 \times 12$ mm^3), and PCC ($20 \times 20 \times 20$ mm^3), shown in Figure 1B. In addition, a whole-brain ROI, defined as the skull-stripped MNI brain template, was included. To obtain ROIs positioned in the same location in the B_1^+ maps of each participant, the T_1-weighted images were registered to the lower-resolution $|B_1^+|$ maps acquired in quadrature with an affine transformation, and to MNI template space using skull-stripping followed by a nonlinear warp transformation (FSL[24]) (Supporting Information Figure S1). The ROIs were then transformed from MNI space, through the T_1-weighted anatomical images, to the lower-resolution set of eight individual channel B_1^+ maps for each data set (Figure 1C) by applying the inverse of the successive transformations.
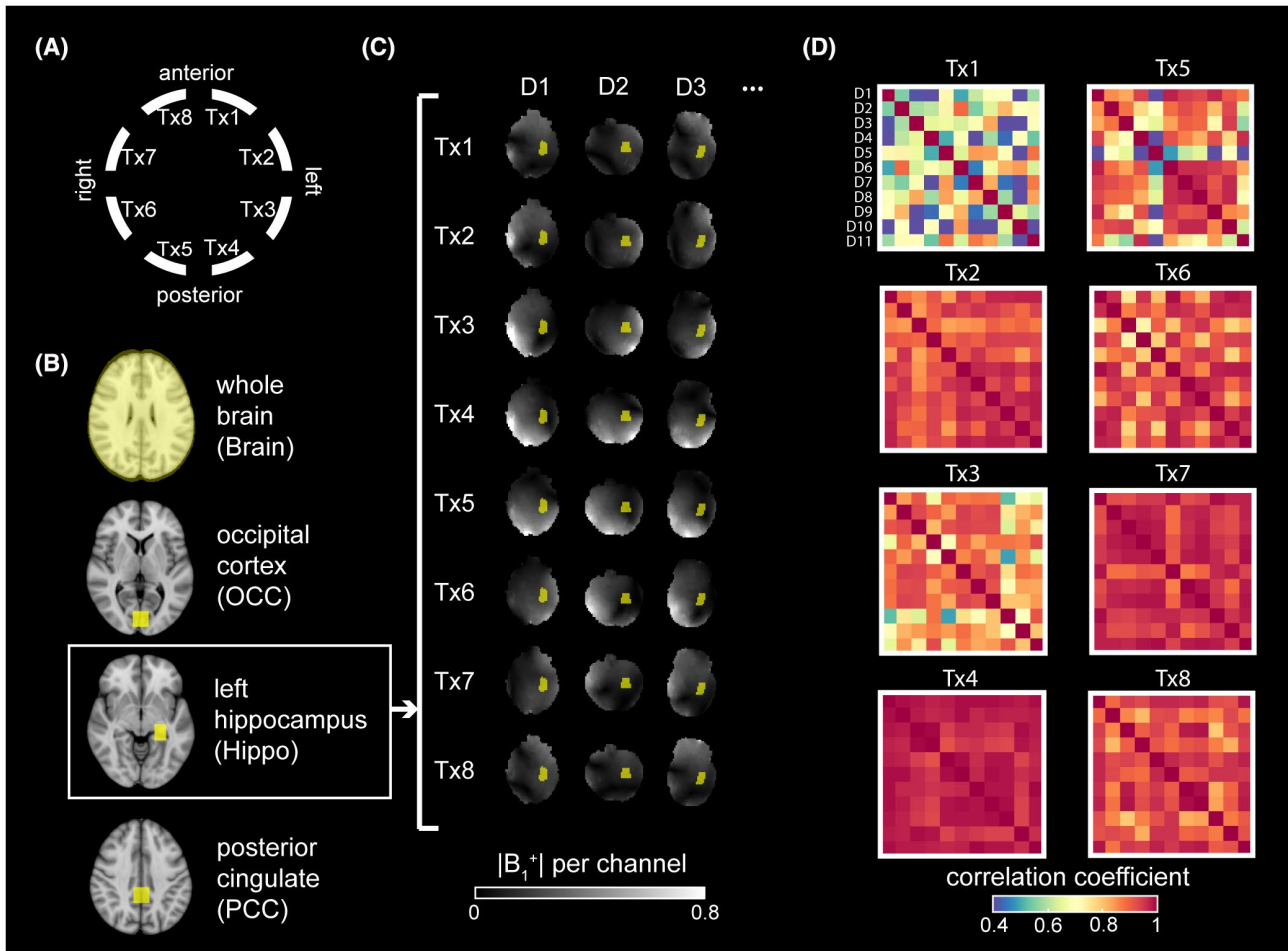
FIGURE 1 A, Schematic of the eight transmit channels (Tx 1-8) on the head coil. B, Predefined regions of interest (ROIs) (in yellow overlay) defined in Montreal Neurological Institute (MNI) space including the whole brain (Brain) and three target ROIs of occipital cortex (OCC), left hippocampus (Hippo), and posterior cingulate (PCC) for MRS. C, Registration of the Hippo ROI from (B) into the participant's $|B_1^+|$ map for each Tx channel shown for three data sets from the database (D1-D3). D, B_1^+ correlation matrices for each Tx channel, showing the pairwise B_1^+ correlation between each subject in the database for the Hippo ROI

3.3 | Shim calculation

Tailored RF shimming at the console and offline joint optimization using the minimax approach for calibration-free shimming (Equation 2) were performed using custom-written code in *MATLAB* (MathWorks, Natick, MA). Constrained optimization was performed using the interior-point algorithm in *fmincon*. For tailored shimming on the scanner, the ROI for RF shimming extended beyond the MRS voxel by about 2 mm in each direction. Vendor-provided constraints on peak and average RF power were 2 kW and 1 W per channel, respectively. Average power was monitored on the scanner using vendor-provided power-monitoring software.

Shim weights from tailored and calibration-free shimming (Equations 1 and 2) were scaled to that of the quadrature mode excitation. In quadrature mode, the B_1^+ amplitude on each channel is the same (defined here as unity), and the phase of each channel is incremented by 45° moving around the eight elements on the cylindrical coil surface.

3.4 | B_1^+ correlation

To assess the degree of similarity in B_1^+ between each participant in the database, a correlational analysis was performed. The B_1^+ maps for each channel were registered to MNI space and then masked by each ROI. For each Tx channel (Tx 1-8), the complex B_1^+ distribution within the ROI was correlated between participants in a pixel-wise manner and the Pearson correlation calculated (Figure 1D). As a summary statistic, the mean and SDs of these pairwise correlation coefficients averaged over all participants ($i \neq j$), $\overline{\rho}$, were calculated using Fisher transformation.

3.5 | *Statistical comparison*

The predicted $|B_1^+|$ and RMS error (RMSE) in each target ROI were compared following quadrature, tailored-free and

calibration-free RF shimming using paired-sample t-test with a significance threshold of .05.

3.6 | *Magnetic resonance spectroscopy*

For the test participants (T1-T4), MRS data were additionally acquired in regions corresponding to the three target ROIs using quadrature, tailored RF shimming, and calibration-free shim weights. In addition, $|B_1^+|$ maps were acquired using the RF shim settings. Magnetic resonance spectroscopy was acquired using STEAM localization and identical parameters for each target region (TE = 14 ms, TR = 4-5 seconds, number of transients = 48-64, pulse bandwidth = 5.7 kHz, pulse duration = 7.3 ms, peak B_1 = 15 μT, and VAPOR [variable power RF pulses with optimized relaxation delays] water suppression[25]). The MRS voxels were manually positioned during examination. Spectra acquired from all receive channels were coil-combined, and then frequency-corrected and phase-corrected before averaging. The SNR was measured in the frequency domain as the height of the NAA peak divided by the SD of the RMS noise in the 10-12-ppm range. Before the MRS acquisition for each region, local B_0 shimming was performed to second-order using a vendor-provided projection-based routine. The B_0 shimming was performed using RF shims without adjustment to channel amplitudes, to ensure sufficient signal outside of the ROI for the projection-based method. For each ROI, B_0 shim settings were held fixed when acquiring spectra using calibration-free and tailored RF shimming.

3.7 | Specific absorption rate modeling

The SAR calculation for different shim modes was carried out using finite-difference time-domain electromagnetic simulations provided by Nova Medical (computed with XFdtd; Remcom, State College, PA). Three-dimensional vector magnetic (B_1) and electric-field values were available for the Duke and Ella dielectric head models computed on a $28 \times 28 \times 28$ cm^3 grid of resolution $2 \times 2 \times 2$ mm^3. For all shim settings, data were scaled using available scattering parameters, such that the total forward power across all channels was 8 W. In quadrature mode, this scaling corresponded to an average $|B_1^+|$ over the central transverse slice of 1 μT for both Duke and Ella models.

To calculate the SAR for different RF shim settings, the Q-matrix approach was used.[26,27] Q-matrices were calculated at each position, r, using electric field, mass density, and electrical conductivities.[28] Local SAR can then readily be computed by multiplication with the desired shim vector, $SAR(r) = w^H Q(r) w$. By averaging over all Q-matrices, a global Q-matrix, and hence mean head SAR, can be obtained for the whole model. Local $10g$ SAR was calculated at each position in the model. The $10g$ cuboidal regions were found

using an iterative approach,[29] and regions with a large proportion (> 20%) of zero-mass voxels were rejected. Local SAR was then calculated using a weighted sum of the Q-matrices within each $10g$ region. The SAR computations were carried out on a high-performance computing cluster (2×20 core processors and 192 GB RAM). The RF duty cycle was assumed to be 100%. The SAR (in W/kg) was computed relative to the B_1^+ field measured in quadrature for both models.

3.8 | *Cross validation*

To estimate the effect of database size on the performance of the calibration-free RF shims, a cross-validation simulation was performed. The size of the database was incremented from $N = 1$ to $N = 11$. At each increment, calibration-free shims for every possible combination of N training data were calculated, and the resulting B_1^+ maps for three test data sets were evaluated. The $|B_1^+|$ and RMSE were calculated and averaged over all combinations for each increment of database size.

4 | RESULTS

4.1 | B_1^+ correlations across database participants

For each ROI, the pairwise correlation of B_1^+ across the ROIs among all ($N = 11$) data sets in the database was measured for each Tx (shown for Hippo ROI in Figure 1D). The mean values of these correlation coefficients, averaged across the 11 subjects in the database, are shown for each ROI in Figure 2. The B_1^+ over the whole-brain ROI was well-correlated among subjects for all Tx channels (minimum $\overline{\rho} = 0.64$ for Tx 4; maximum $\overline{\rho} = 0.72$ for Tx 7). When considering the three target ROIs, the mean B_1^+ correlation across the database participants was generally weakest within the OCC (Tx 2 gave minimum $\overline{\rho} = 0.36$; Tx 8 had highest $\overline{\rho} = 0.89$). The B_1^+ correlation within the left Hippo and PCC ROIs were higher than the OCC and followed similar trends across channels: Hippo (minimum $\overline{\rho} = 0.62$ on Tx 1; maximum $\overline{\rho} = 0.97$ on Tx 4) and PCC (minimum $\overline{\rho} = 0.76$ on Tx 7; maximum $\overline{\rho} = 0.98$ on Tx 6).

4.2 | *Static RF shim solutions*

The static RF shim weights arising from tailored shimming (Equation 1) for the database participants (D1-D11) are shown on a polar plot in Figure 3A for all three target ROIs. Further details are provided in Supporting Information Figure S2. The RF shim amplitudes are scaled relative to quadrature mode. Corresponding solutions for whole-brain
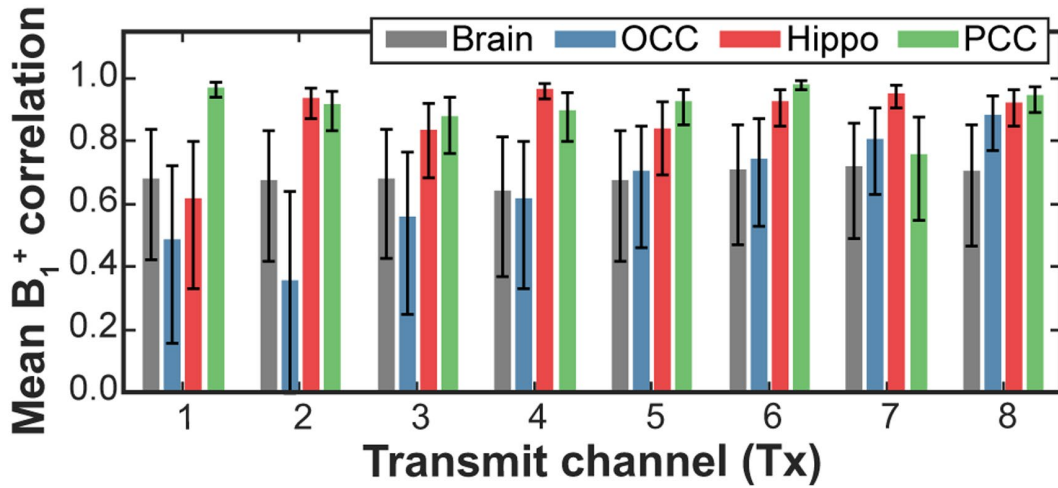
FIGURE 2 Mean regional correlation coefficients of B_1^+ on each channel across the 11 participants in the database (D1-D11). Correlations were determined for the Brain and three target regions: OCC, Hippo, and PCC. Error bars represent the SEM across correlation coefficients determined following Fisher's *z* transformation
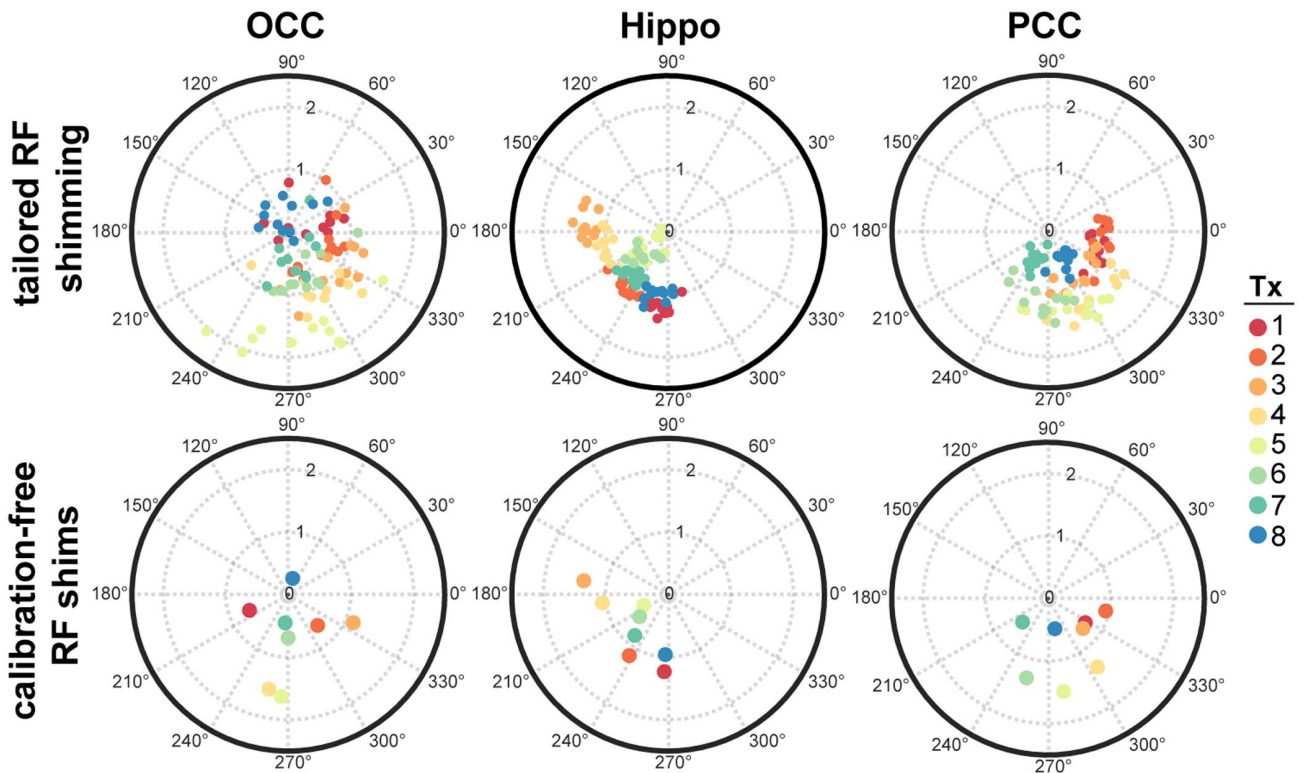
FIGURE 3 Radiofrequency shims (phase and amplitude) on each Tx channel calculated for the three different ROIs when applying tailored shimming across B_1^+ maps in 11 different subjects (top) and for calibration-free shims produced by optimization over the whole database (bottom). The RF shim amplitudes are scaled such that in quadrature mode the amplitude on each channel is 1

RF shimming are provided in Supporting Information Figure S3. For tailored shimming, OCC shims showed the greatest variation among database participants in channel phase (SD: 95°, Tx 8) and amplitude (SD: 0.26, Tx 1) of any target ROI.

The calibration-free static RF shims (Equation 2), calculated over the database participants, are shown in Figure 3B for all three target ROIs. The distribution of channel phases for each ROI approximately matched that of tailored shimming (Figure 3A). The OCC calibration-free shim weights had the largest single-channel amplitude (maximum $|w_i| = 1.64$, Tx 5), and the mean relative phase among neighboring transmit elements was 81°, 93°, and 32° for OCC, Hippo, and PCC, respectively.

4.3 | Predicted $|B_1^+|$

The predicted $|B_1^+|$ was calculated in each ROI using the tailored and calibration-free shims and compared with the quadrature mode values (Figure 4) for the database subjects (D1-D11). Calibration-free RF shims led to statistically similar $|B_1^+|$ levels in all three target ROIs compared with tailored RF shimming. When comparing tailored to calibration-free shimming for the database subjects, there was no significant difference among mean $|B_1^+|$ in the ROIs in OCC (0.99 vs 0.96, $p = .15$), left Hippo (0.97 vs 0.96, $p = .5$), or PCC (0.93 vs 0.93, $p = .98$). However, there was a difference in $|B_1^+|$ in the whole-brain ROI for tailored compared with the calibration-free approach (0.73 vs 0.66, $p < 1^{-4}$).

The RMSEs of predicted $|B_1^+|$ from the target over the ROIs are also plotted. There were small, but significant differences in RMSE in OCC (0.06 vs 0.12, $p < 1^{-5}$), Hippo (0.05 vs 0.06, $p < 1^{-4}$), and PCC (0.10 vs 0.13, $p = .02$) ROIs as well as whole brain (0.36 vs 0.41, $p < 5^{-4}$) when

using tailored versus calibration-free shimming, suggesting an increased variability in $|B_1^+|$ across the ROI for the calibration-free case. As expected, RF shimming led to significantly reduced RMSEs and higher $|B_1^+|$ in all three target ROIs compared with quadrature mode operation. For the whole-brain ROI, calibration-free shims did not lead to an improved RMSE compared with quadrature mode ($p = .94$).

The same comparison was performed on the B_1^+ maps acquired in the test data set (T1-T4) (ie those participants who were not included in the database optimization). After applying calibration-free shims, the mean $|B_1^+|$ in the test data set after calibration-free shimming was statistically similar to that obtained in the database subjects for all ROIs (OCC: 1.0, $p = .06$; Hippo: 1.0, $p = .3$; PCC: 0.99, $p = .29$; whole brain: 0.65, $p = .8$). In addition, the RMSE was statistically similar to that obtained in the database subjects for all regions: OCC (0.14, $p = .4$), Hippo: (0.06, $p = .95$), PCC (0.10, $p = .09$), whole brain (0.4, $p = .6$).
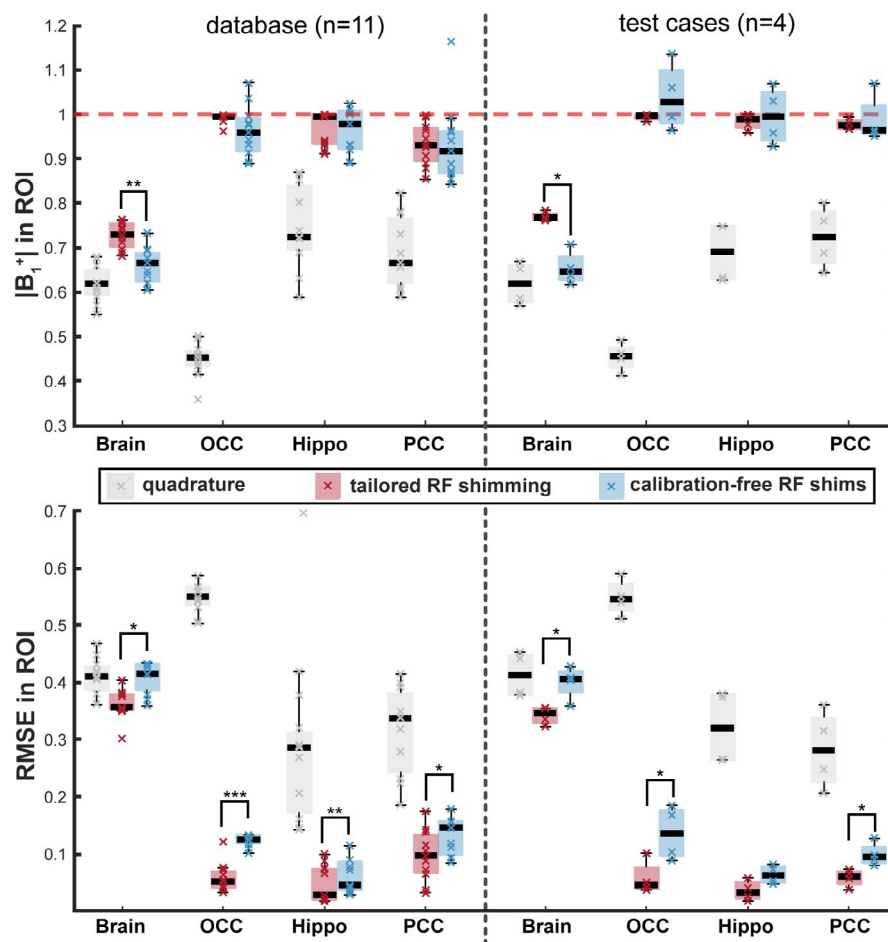
FIGURE 4 Predicted mean $|B_1^+|$ and RMS error (RMSE) in all ROIs (Brain, OCC, Hippo, and PCC), calculated after relevant RF shim was applied (tailored or calibration-free). Analysis was performed on the database (left) and the test data sets (right). Red horizontal dotted line indicates the target value of $|B_1^+| = 1$. The RMSE and $|B_1^+|$ were significantly different for all ROIs with RF shimming compared with quadrature mode (statistical comparison shown between tailored and calibration-free shims) (*$p < .05$; **$p < $ 1E-4, ***$p < $ 1E-5). Lines through each bar indicate the median value, and shaded region represents 25th to 75th percentiles

Figure 5 shows $|B_1^+|$ maps acquired in vivo in subjects T1-T4 using calibration-free and tailored shims for the PCC ROI, as well as using quadrature mode operation. Calibration-free shims generated a pattern of $|B_1^+|$ inside the target ROI and across the whole brain, which was reproducible across subjects (T1-T4) for all target ROIs.

4.4 | Spectral profile and SNR

Spectra from a representative test subject (T3) are shown in Figure 6, and spectra from other subjects are provided in Supporting Information Figure S4. Spectra acquired in all ROIs using calibration-free RF shimming were of excellent quality and all showed a small residual water peak. Spectral profiles for tailored and calibration-free shimming were remarkably similar, even for the challenging Hippo region. Using the power settings applied across shim modes in this work, it was not possible to obtain metabolite spectra from the OCC region in all test subjects when operating in quadrature mode (mean $|B_1^+| = 0.45 \pm 0.04$) due to a lack of $|B_1^+|$ signal for adequate water suppression. In addition, the lack of $|B_1^+|$ also affected the performance of the projection-based B_0 shimming algorithm, as evidenced by the broad asymmetric water peak. The mean spectral SNR

obtained with tailored RF shimming was not significantly different from that obtained with calibration-free shims: 119 ± 6 versus 122 ± 15 in OCC ($p = .54$), 50 ± 3 versus 49 ± 3 in Hippo ($p = .27$), and 108 ± 30 versus 110 ± 34 in PCC ($p = .86$). Overall, there was no detectable difference in spectral quality between tailored and calibration-free shimming.

4.5 | Effect of database size

The influence of the size of the database used in calculating the calibration-free shims was estimated using a cross-validation approach, and the results are shown in Figure 7 for the three target ROIs. As the number of data sets for calibration-free shim calculation increased from 1 to 11, the mean $|B_1^+|$ remained close to the target value, even with few available data sets. The mean RMSE in all target ROIs appeared to plateau. There was a consistent reduction in RMSE for the OCC target ROI with inclusion of up to six data sets, beyond which the gains in RMSE diminished. The PCC and Hippo ROIs, however, did not show a decrease in RMSE with increasing number of data sets. In fact, the inclusion of only a single data set was sufficient to reach a stable RMSE value in these ROIs.
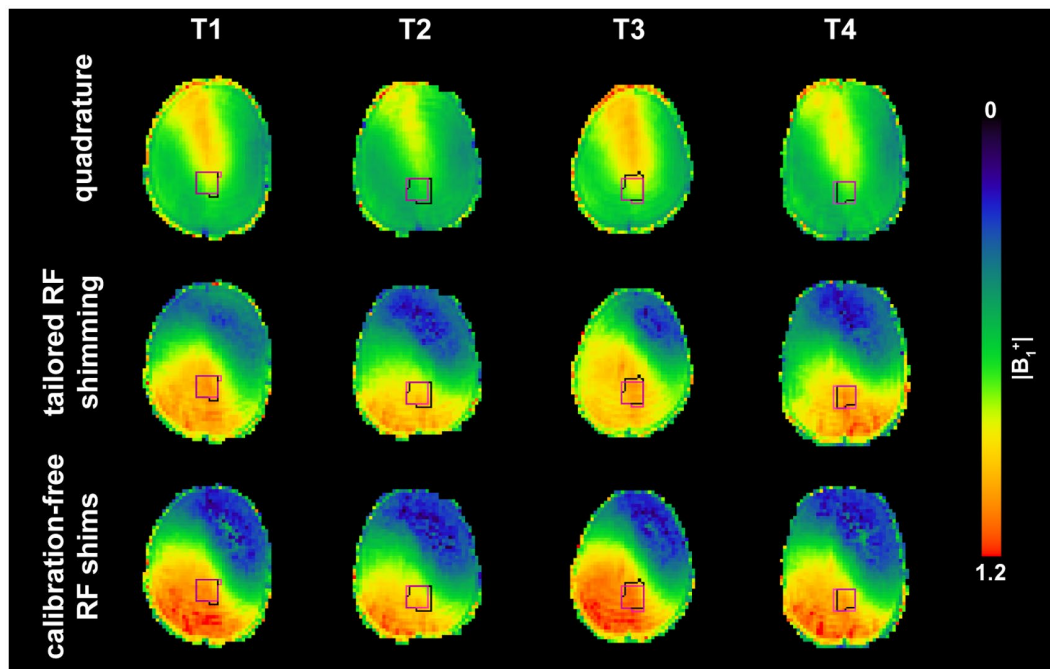
FIGURE 5 $|B_1^+|$ maps (shown for a transverse slice) acquired from four test data sets (T1-T4) outside of the database. Data were acquired with three different RF channel weightings for PCC acquisition. The final row is acquired with the calibration-free shims. The black outline is the calibration-free target ROI in the B_1^+ space of each participant. The magenta outline shows the position of the MRS voxel. Images were skull-stripped
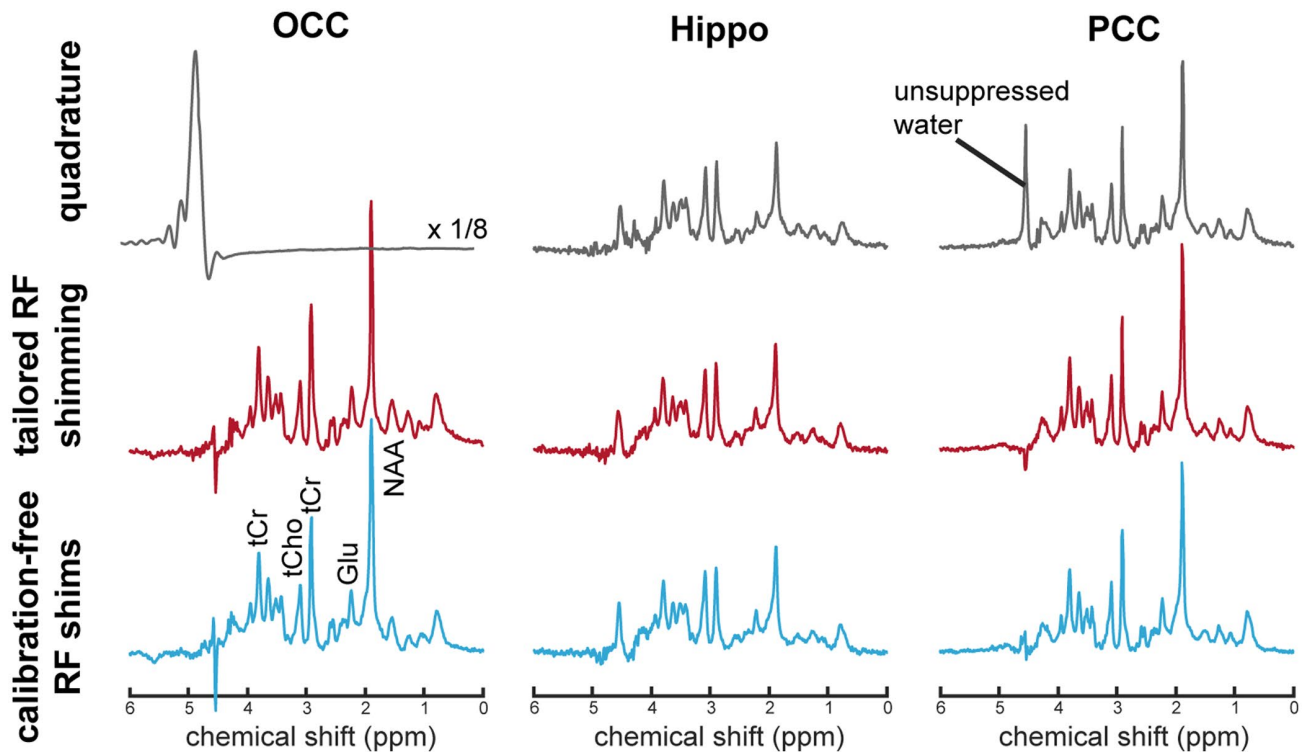
FIGURE 6   Spectra acquired in 1 subject (T3) from the three ROIs using quadrature-mode operation and tailored and calibration-free RF shim settings. Spectra were Gaussian-filtered ($\sigma^2 = 0.2$) for display only. A lack of $|B_1^+|$ led to large visible unsuppressed water signal, particularly in quadrature mode. Abbreviations: Glu, glutamate; NAA, N-acetylaspartate; tCho, total choline; tCr, total creatine;

4.6 | *Specific absorption rate*

Simulations of SAR deposition using the calibration-free shim settings were carried out on standard dielectric head models, Duke and Ella. Figure 8 shows a map of the average local $10g$ SAR for both models after the Hippo ROI calibration-free RF shims were applied, with results scaled to the same total transmitted power as in quadrature mode. The pattern and location of hotspots was similar for both dielectric models. Maximum local $10g$ SAR using these shim settings was closely matched between models: 3.79 W/kg and 3.74 W/kg for Duke and Ella, respectively. This was 84% (4.51 W/kg) and 75% (4.99 W/kg) of the respective maximum $10g$ SAR values obtained in quadrature mode. The SAR maps for the OCC and PCC ROIs are provided in Supporting Information Figure S5.

A summary of the SAR results is given in Table 1. Average head SAR deposition using calibration-free shims was less than in quadrature mode for both models, with a maximum average head SAR of 0.93 W/kg for OCC in Ella (65% of quadrature mode). The lowest total head SAR was observed in the Duke model using the Hippo calibration-free shims (0.66 W/kg; 52% of quadrature). Across all ROIs, calibration-free shims produced lower maximum local $10g$ SAR deposition than quadrature mode. The PCC shims for Duke gave the highest $10g$ SAR (4.32 W/kg, 96% of quadrature), while the OCC shims for Ella gave the lowest (3.59 W/kg, 72% of quadrature).

5 | DISCUSSION

This work has demonstrated a method of acquiring B_1^+ calibration-free MRS data at 7 T with a commercial pTx coil by designing static RF shim solutions for predefined ROIs, generated from a database of B_1^+ maps and anatomical images. The $|B_1^+|$ generated in small ROIs using calibration-free RF shims was not significantly different than that produced using subject-specific tailored RF shims, even in regions where large B_1^+ variation existed across database participants. The calibration-free shims produced consistent $|B_1^+|$ for a given power setting, so that renormalization of the target flip angle was not required. The approach requires neither B_1^+ mapping, nor prior definition of an RF shimming region, nor numerical optimization at the scanner console, thereby alleviating the time-consuming steps of using pTx. Calibration-free RF shims led to spectra of excellent quality, with adequate water suppression and comparable SNR to that obtained using tailored RF shimming. By their nature, calibration-free RF shims allowed more predictable and easier offline SAR modeling than tailored shims, and led to more consistent B_1^+ patterns across the brain. Reduced global and local $10g$ SAR was generated for the same total transmitted power when using the calibration-free shims compared with quadrature mode, suggesting that transmit power could be increased. It is anticipated that this method could be extended to any small ROI. Consequently, calibration-free

(A)

(B)
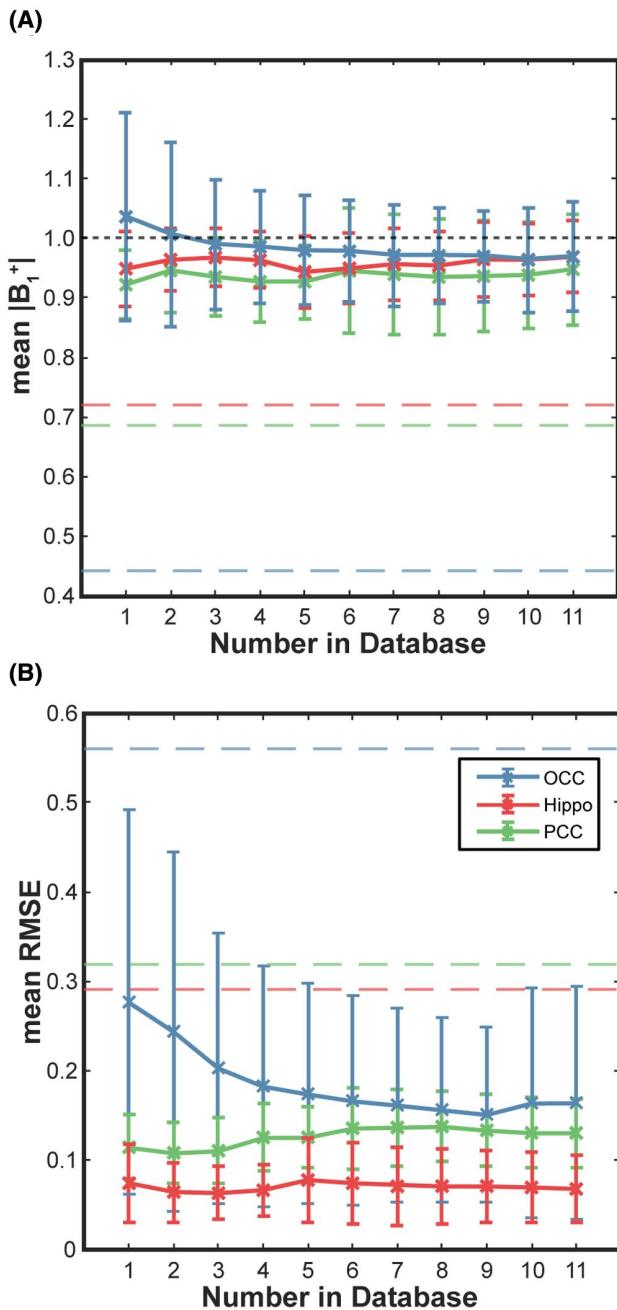
FIGURE 7 Mean $|B_1^+|$ (A) and mean RMSE (B) after the calculation and application of calibration-free RF shims with increasing number of B_1^+ maps in the database. The simulation was carried out as a cross-validation from a total of 15 available B_1^+ maps, with each iteration using three test data sets. Dashed line indicates average RMSE in region when run in quadrature mode across the simulated data sets. Black dotted line is target $|B_1^+| = 1$

static RF shims may increase the practical advantage of pTx for ultrahigh-field MRS, while cutting down scan time, to make such measurements more clinically viable.

Static RF shim solutions were sufficient to generate reproducible $|B_1^+|$ profiles across participants in small target ROIs for single-voxel MRS, yet mean $|B_1^+|$ in the larger whole-brain ROI was far below the desired value and was worse

for calibration-free shims than tailored shimming. This is in line with the inferior performance of static RF shimming over whole-brain ROIs in the work of Gras et al[14] and with simulations performed by Mao et al, reporting that RF shimming is more effective for small ROIs.[19] Although mean pairwise B_1^+ correlation among database participants for the whole-brain ROI in the current study was lower (0.64, worst case) than that of Gras et al (0.82, worst case), calibration-free shim solutions could be readily found to produce comparable $|B_1^+|$ availability in small ROIs to tailored RF shimming. The lower correlations in this study may be due to variation in head position relative to RF coil elements and head size of the participants, which was not controlled for as the database was formed. Considering B_1^+ correlations within the three target ROIs, the worst-case agreement was observed in the OCC region. The OCC also required more subjects in the database to reach a stable RMSE compared with the other two regions when calculating the optimal calibration-free shims (Figure 7), and the OCC had a larger variation in RF shim phases and amplitudes when applying tailored shimming. As a result, OCC measurements showed the greatest benefit from B_1^+ shimming, similar to previous findings.[10] The OCC is the most inferior and peripheral of all the target ROIs studied, and showed the lowest $|B_1^+|$ when running in quadrature mode, due to the loss of peripheral B_1^+ from destructive interferences in head using volume transmit coils.[2] The OCC is closest to the coil elements, so it is likely that participant head position in the coil varies in the coronal (left–right) and sagittal (anterior–posterior) planes. Thus, the relative position of the OCC with respect to the coil elements is presumably most variable.

Calibration-free shims were calculated with an a priori constraint on the total power summed across all transmit elements. The total power was fixed at a value determined experimentally, such that when applying RF shimming using the pulses and timings of the sequences used, the average power through any channel remained less than 1 W per channel (the vendor-determined average safety limit). By choosing the total power of the shim solution a priori, based on safety limits for a given sequence, more efficient use of power is not possible and therefore is a limitation of this work. A consequence of fixing the power for all acquisition modes to fall below vendor-provided safety limits for RF shimming is that quadrature-mode performance may have been improved by increasing the input power to achieve a desired $|B_1^+|$. Conversely, by relaxing the total power used in RF shimming, the target $|B_1^+|$ in any ROI may have been reached using less power than presented here. An equal power setting across acquisition modes, however, allowed for accurate comparison of $|B_1^+|$ and RMSE for the same input power. In general, the approach presented here is flexible and may be applied with different shimming strategies. In the future, a softer constraint on total power during the shim optimization
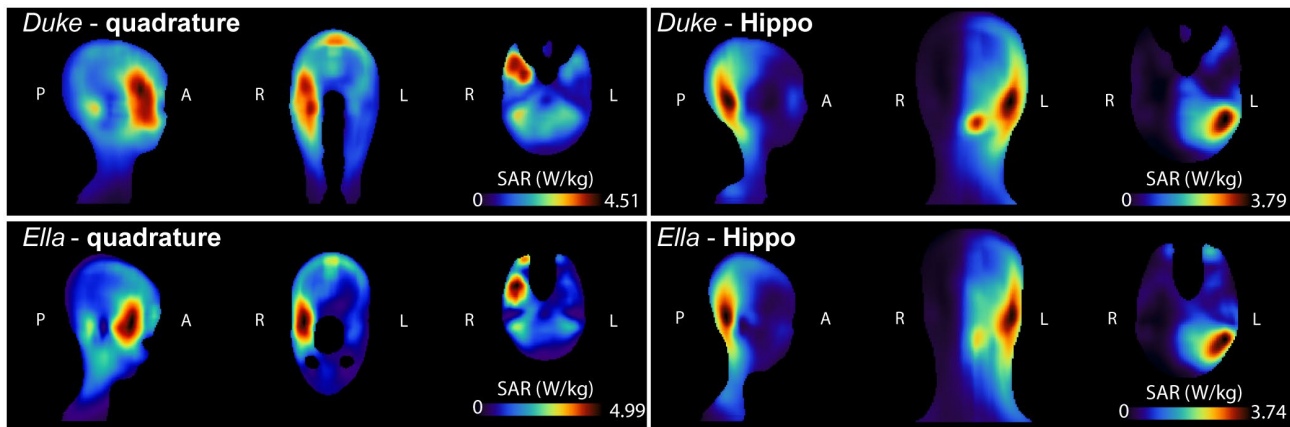
FIGURE 8 Average local 10g specific absorption rate (SAR; W/kg) simulated for the Duke and Ella dielectric head models after the calibration-free RF shim for the Hippo ROI was applied. The RF shim weights for SAR estimation are normalized at a fixed total power of 8 W, which generated a |B_1^+| of 1 μT across the central slice in quadrature mode. The sagittal, coronal, and axial slices shown intersect at the maximum local 10g SAR (Duke, 3.79 W/kg; Ella, 3.74 W/kg). Abbreviations: A, anterior; L, left; P, posterior; R, right

TABLE 1 Summary of SAR simulations for quadrature-mode and calibration-free RF shims in OCC, Hippo, and PCC in Duke and Ella models

Shim	Model	Head SAR (W/kg)	% of Quad	Max 10g SAR (W/kg)	% of Quad	Location (x, y, z) (image pixels)
Quad	Duke	1.27	–	4.51	–	(90, 85, 54)
	Ella	1.44	–	4.99	–	(92, 79, 66)
OCC	Duke	0.82	65%	3.55	79%	(72, 59, 88)
	Ella	0.93	65%	3.59	72%	(65, 32, 63)
Hippo	Duke	0.66	52%	3.79	84%	(95, 47, 66)
	Ella	0.70	48%	3.74	75%	(96, 46, 64)
PCC	Duke	0.71	56%	4.32	96%	(69, 49, 80)
	Ella	0.85	59%	4.47	90%	(71, 48, 81)

Note:: The head SAR was averaged over the whole model.

Abbreviations: max, maximum; quad, quadrature mode.

may be more appropriate, in addition to taking into account sequence-specific parameters to allow more efficient use of power.[30] Further work should also investigate the combination of dielectric padding and static RF shimming, similar to a previous study.[31] Such an approach may enable more efficient use of available transmit power for small ROIs, although differences in pad positioning may introduce variability in the B_1^+ database for the approach outlined in this work.

RF shimming strategies can produce lower global and local SAR than quadrature excitation, as predicted from the targeted use of available B_1^+.[28,32] This finding was confirmed in the current work, in which head SAR and local 10g SAR were considerably lower using calibration-free optimized RF shims, compared with quadrature mode using equal power settings. If accounting for optimal power conditions (ie, to achieve |B_1^+| = 1 in the ROI), then the difference in estimated SAR would be even greater. For example, for PCC, a factor of 1.07 and 1.49 increase in power would be required (Figure 4) using calibration-free shims and in quadrature mode, respectively. The OCC calibration-free

RF shims produced the highest head SAR (0.93 W/kg) out of all ROIs, yet lowest maximum local 10g SAR (3.55 W/kg). Interestingly, OCC shims had the largest single-channel amplitude (Figure 3). The smallest mean phase difference among neighboring transmitter channels was for the PCC calibration-free shims, which also produced the highest local 10g SAR.

The spatial distribution of calculated head SAR using calibration-free shims was similar across models, and local hotspots overlapped with the target ROI. This is important, as SAR information is not readily available during a scan, and therefore conservative power settings are often used when performing RF shimming,[32] as was the case in the current work. However, calibration-free shimming can be used in conjunction with offline SAR modeling to provide better estimates of local and global SAR, allowing higher transmit power to be tolerated. Thus, the advantages of pTx may be more readily realized. Ideally, SAR variance would be calculated directly using models developed from database participants to determine power safety margins. That was not

possible in this work, however, as precise coil models were not available.

The results for the whole-brain ROI showed that as the size of the target ROIs increases, such as over a large MRSI grid, static RF shimming alone is not able to produce desirable solutions, and the inclusion of RF and gradient waveform optimization is required. However, the design of large flip-angle spoke pulses,[33] which have a broad frequency profile to reduce chemical-shift displacement for MRS, is nontrivial.[34] Therefore, additional work is needed to design broadband spokes pulses, for the universal approach to be applied to larger ROIs in MRS.

The use of a template ROI definition combined with nonlinear registration was chosen to avoid manually prescribing the database ROIs over variable anatomies and head positions. Additionally, this approach allows calibration-free shims to be automatically generated from any arbitrary-shaped ROI. In the current work, there was a high degree of overlap between the automatically registered ROIs and the manually positioned MRS voxels (Figure 5). Despite expected deformations of the cuboidal template ROIs after nonlinear registration (Supporting Information Figure S1 and Figure 5), the shim solutions produced B_1^+ fields that varied smoothly on the length scale of the MRS voxel. Thus, it is expected that subvoxel deviations in position or ROI shape will not significantly affect the results presented here. However, to reduce any errors arising from a mismatch in voxel placement and ROI definition, automatic voxel placement[35] may be used and could exploit identical template definitions for shim optimization and MRS placement, ensuring maximal overlap.

Finally, it is expected that, as with universal k_T-pulses, calibration-free static RF shim settings may be applicable across sites for the same coil and head position, and the approach may be extended to different organs. In practice, it is envisaged that a dictionary of shims for commonly measured regions could be generated offline once the database of B_1^+ maps has been acquired. The calibration-free shims generated following this one-off optimization could be loaded onto the scan console such that the scanner operator may simply choose the appropriate shim settings corresponding to the target anatomy. Because the provided scans are run at the same power setting as the optimization, there is no need to perform B_1^+ mapping or further optimization at the scanner console, and scan time is purely limited by the length of the acquisition sequence. If desired, standard RF power adjustment could be performed while using the predetermined shim weights, to fine-tune the power on a subject-wise basis.

6 | CONCLUSIONS

Static RF shims calculated offline over a database of participants for predefined ROIs produced high-quality MR spectra at ultrahigh field. Results were similar to those produced by performing tailored RF shimming on each participant and region separately, but the scanning time was reduced in the case of the calibration-free shims because B_1^+ mapping and online shim calculation were not required. The resulting SAR deposition from calibration-free shims was lower than in quadrature mode, and intrinsically more predictable than when tailoring the shimming for each participant, suggesting that such shims could be implemented using higher power constraints than typically imposed on RF shimming in most pTx systems. As a result, the practical ease and utility of pTx for ultrahigh-field MRS studies is significantly improved using the calibration-free approach.

DATA AVAILABILITY STATEMENT
Code for calculation of calibration-free RF shims is available at github.com/aberrington/calibfreeRFshim.

ORCID
Adam Berrington https://orcid.org/0000-0002-1207-8193

TWITTER
Adam Berrington @adamberrington

REFERENCES
1. Vaughan JT, Garwood M, Collins CM, et al. 7T vs. 4T: RF power, homogeneity, and signal-to-noise comparison in head images. *Magn Reson Med*. 2001;46:24-30.
2. Van de Moortele P-F, Akgun C, Adriany G, et al. B(1) destructive interferences and spatial phase patterns at 7 T with a head transceiver array coil. *Magn Reson Med*. 2005;54:1503-1518.
3. Kreis R. Issues of spectral quality in clinical 1H-magnetic resonance spectroscopy and a gallery of artifacts. *NMR Biomed*. 2004;17:361-381.
4. Deelchand DK, Iltis I, Henry P-G. Improved quantification precision of human brain short echo-time 1 H magnetic resonance spectroscopy at high magnetic field: a simulation study. *Magn Reson Med*. 2014;72:20-25.
5. Tkáč I, Öz G, Adriany G, Ugurbil K, Gruetter R. In vivo 1H NMR spectroscopy of the human brain at high magnetic fields: metabolite quantification at 4T vs. 7T. *Magn Reson Med*. 2009;62:868-879.

6. Ibrahim TS, Lee R, Baertlein BA, Kangarlu A, Robitaille PML. Application of finite difference time domain method for the design of birdcage RF head coils using multi-port excitations. *Magn Reson Imaging*. 2000;18:733-742.

7. Katscher U, Börnert P, Leussler C, Van den Brink JS. Transmit SENSE. *Magn Reson Med*. 2003;49:144-150.

8. Padormo F, Beqiri A, Hajnal JV, Malik SJ. Parallel transmission for ultrahigh-field imaging. *NMR Biomed*. 2016;29:1145-1161.

9. Metzger GJ, Snyder C, Akgun C, Vaughan T, Ugurbil K, Van de Moortele P-F. Local B1+ shimming for prostate imaging with transceiver arrays at 7T based on subject-dependent transmit phase measurements. *Magn Reson Med*. 2008;59:396-409.

10. Emir UE, Auerbach EJ, Van de Moortele P-F, et al. Regional neurochemical profiles in the human brain measured by 1H MRS at 7 T using local B1 shimming. *NMR Biomed*. 2012;25:152-160.

11. Deniz CM, Brown R, Lattanzi R, Alon L, Sodickson DK, Zhu Y. Maximum efficiency radiofrequency shimming: theory and initial application for hip imaging at 7 tesla. *Magn Reson Med*. 2013;69:1379-1388.

12. Setsompop K, Wald LL, Alagappan V, Gagoski BA, Adalsteinsson E. Magnitude least squares optimization for parallel radio frequency excitation design demonstrated at 7 Tesla with eight channels. *Magn Reson Med*. 2008;59:908-915.

13. Boer V, Klomp D, Juchem C, Luijten P, de Graaf R. Multi-slice MRSI of the human brain at 7 tesla using dynamic B 0 and B 1 shimming. *Magn Reson Imaging*. 2012;116:662-670.

14. Gras V, Vignaud A, Amadon A, Le Bihan D, Boulant N. Universal pulses: a new concept for calibration-free parallel transmission. *Magn Reson Med*. 2017;77:635-643.

15. Gras V, Mauconduit F, Vignaud A, et al. Design of universal parallel-transmit refocusing k T -point pulses and application to 3D T 2 -weighted imaging at 7T. *Magn Reson Med*. 2018;80:53-65.

16. Geldschläger O, Shao T, Henning A. Universal parallel transmit pulse design for 3-dimensional local-excitation: a 9.4T simulation study. In: *Proceedings of the 27th Annual Meeting of the ISMRM, Montreal*, Canada, 2019. p 4639.

17. Tomi-Tricot R, Gras V, Thirion B, et al. SmartPulse, a machine learning approach for calibration-free dynamic RF shimming: preliminary study in a clinical environment. *Magn Reson Med*. 2019;82:2016-2031.

18. Ianni JD, Cao Z, Grissom WA. Machine learning RF shimming: prediction by iteratively projected ridge regression. *Magn Reson Med*. 2018;80:1871-1881.

19. Mao W, Smith MB, Collins CM. Exploring the limits of RF shimming for high-field MRI of the human head. *Magn Reson Med*. 2006;56:918-922.

20. Nistler J, Diehl J, Renz W, Eberler L. Homogeneity improvement using a 2 port birdcage coil. In: *Proceedings of the 15th Annual Meeting of the ISMRM*, Berlin, Germany, 2007. p 1063.

21. Geppert C, Nistler J, Renz W, Panagiotelis I, Speckner T. Reduced B1-inhomogeneities in breast MRI using optimized RF excitation. *In: Proceedings of the 16th Annual Meeting of the ISMRM*, Toronto, Canada, 2008. p 2726.

22. Nehrke K, Börnert P. DREAM-a novel approach for robust, ultrafast, multislice B1 mapping. *Magn Reson Med*. 2012;68:1517-1526.

23. Van de Moortele P-F, Snyder C, DelaBarre L, Adriany G, Vaughan JT, Ugurbil K. Calibration tools for RF shim at very high field with multiple element RF coils: from ultra fast local relative phase to absolute magnitude B1+ mapping. *In: Proceedings of the Joint Annual Meeting of ISMRM-ESMRMB, Berlin, Germany*, 2007.

24. Jenkinson M, Beckmann CF, Behrens TEJ, Woolrich MW, Smith SM. FSL. *NeuroImage*. 2012;62:782-790.

25. Tkáč I, Starčuk Z, Choi IY, Gruetter R. In vivo 1H NMR spectroscopy of rat brain at 1 ms echo time. *Magn Reson Med*. 1999;41:649-656.

26. Bardati F, Borrani A, Gerardino A, Lovisolo GA. SAR optimization in a phased array radiofrequency hyperthermia system. *IEEE Trans Biomed Eng*. 1995;42:1201-1207.

27. Graesslin I, Homann H, Biederer S, et al. A specific absorption rate prediction concept for parallel transmission MR. *Magn Reson Med*. 2012;68:1664-1674.

28. Homann H, Graesslin I, Eggers H, et al. Local SAR management by RF Shimming: a simulation study with multiple human body models. *Magn Reson Mater Physics, Biol Med*. 2012;25: 193-204.

29. Volakis JL, Caputa K, Okoniewski M, Stuchly MA. An algorithm for computations of the power deposition in human tissue. *IEEE Antennas Propag Mag*. 1999;41:102-107.

30. Beqiri A, Price AN, Padormo F, Hajnal JV, Malik SJ. Extended RF shimming: sequence-level parallel transmission optimization applied to steady-state free precession MRI of the heart. *NMR Biomed*. 2017;30:1-15.

31. Brink WM, Van Den Brink JS, Webb AG. The effect of high-permittivity pads on specific absorption rate in radiofrequency-shimmed dual-transmit cardiovascular magnetic resonance at 3T. *J Cardiovasc Magn Reson*. 2015;17:1-8.

32. Van Den Bergen B, Van Den Berg CAT, Klomp DWJ, Lagendijk JJW. SAR and power implications of different RF shimming strategies in the pelvis for 7T MRI. *J Magn Reson Imaging*. 2009;30:194-202.

33. Saekho S, Yip CY, Noll DC, Boada FE, Stenger VA. Fast-kz three-dimensional tailored radiofrequency pulse for reduced B1 inhomogeneity. *Magn Reson Med*. 2006;55:719-724.

34. Setsompop K, Alagappan V, Gagoski BA, et al. Broadband slab selection with B 1 + mitigation at 7T via parallel spectral-spatial excitation. *Magn Reson Med*. 2009;61:493-500.

35. Park YW, Deelchand DK, Joers JM, et al. AutoVOI: real-time automatic prescription of volume-of-interest for single voxel spectroscopy. *Magn Reson Med*. 2018;80:1787-1798.

SUPPORTING INFORMATION

Additional Supporting Information may be found online in the Supporting Information section.

FIGURE S1 Results of non-linear registration of the three target ROIs on T1-weighted anatomical images for the first 5 participants in the database. Yellow box is the ROI

FIGURE S2 Top: Circular deviation of the phase (defined over 0 to 360°) for each transmit channel following tailored shimming of the 11 B1+ maps in the database. Bottom: Standard deviation of the transmit channel amplitudes after tailored shimming on the database

FIGURE S3 RF shims (phase and amplitude) on each transmit channel calculated for the whole brain ROI when applying tailored shimming across B1+ maps in 11 different subjects (top) and for calibration-free shims produced by optimising over the database (bottom)

FIGURE S4 MR spectra acquired in the remaining test participants (T1,T2 and T4) acquired using quadrature mode (grey) and RF shimming using tailored approach (red) calibration-free shims (blue)

FIGURE S5 Local 10g SAR simulated for Duke and Ella head models using the occipital and posterior-cingulate calibration-free RF shims